

# Current induced hidden states in Josephson junctions

Received: 1 July 2024

Accepted: 28 August 2024

Published online: 14 September 2024

 Check for updates

Shaowen Chen  <sup>1,6</sup>✉, Seunghyun Park  <sup>1,6</sup>, Uri Vool  <sup>1,2</sup>, Nikola Maksimovic <sup>1</sup>, David A. Broadway <sup>3</sup>, Mykhailo Flaks <sup>3</sup>, Tony X. Zhou  <sup>1,5</sup>, Patrick Maletinsky  <sup>3</sup>, Ady Stern  <sup>4</sup>, Bertrand I. Halperin  <sup>1</sup> & Amir Yacoby  <sup>1</sup>✉

Josephson junctions enable dissipation-less electrical current through metals and insulators below a critical current. Despite being central to quantum technology based on superconducting quantum bits and fundamental research into self-conjugate quasiparticles, the spatial distribution of super current flow at the junction and its predicted evolution with current bias and external magnetic field remain experimentally elusive. Revealing the hidden current flow, featureless in electrical resistance, helps understanding unconventional phenomena such as the nonreciprocal critical current, i.e., Josephson diode effect. Here we introduce a platform to visualize super current flow at the nanoscale. Utilizing a scanning magnetometer based on nitrogen vacancy centers in diamond, we uncover competing ground states electrically switchable within the zero-resistance regime. The competition results from the superconducting phase re-configuration induced by the Josephson current and kinetic inductance of thin-film superconductors. We further identify a new mechanism for the Josephson diode effect involving the Josephson current-induced phase. The nanoscale super current flow emerges as a new experimental observable for elucidating unconventional superconductivity, and optimizing quantum computation and energy-efficient devices.

Characterization and control over the super current flow is critical for Josephson junctions (JJs)<sup>1–3</sup>, which have become a building block in quantum and classical technology<sup>4–11</sup> while remained a rich area of exploration into fundamental particles<sup>12–14</sup> and unconventional superconductivity<sup>15–17</sup>. Compared to spectroscopic probes that measures the amplitude of the superconducting (SC) wave function<sup>18</sup>, the super current flow encodes the SC phase. Mapping the spatial distribution of super current has revealed the pairing symmetry of unconventional superconductors<sup>19,20</sup>, and recently identified screening current as the source of SC diode effect in SC/ferromagnet structures<sup>21</sup>. In addition, the local super current flow affects device parameters such as the impedance of SC circuits and anharmonicity

of SC qubits due to the change in kinetic inductance<sup>22</sup>. Despite the scientific and technological relevance, direct visualization of the Josephson current flow and its response to external tuning knobs such as bias current and magnetic field remains experimentally beyond reach<sup>18,23–27</sup>. This is mostly due to the sensitive nature of the JJ, which responds to small perturbations and the nanoscale spatial resolution needed to resolve the evolution of the super current flow. To date, JJ characterization has primarily relied on indirect measurements such as the critical current that separates the dissipation-less (zero electrical resistance) and resistive states. However, this only provides insight into the resistive state while the ground state below the critical current stays hidden.

<sup>1</sup>Department of Physics, Harvard University, Cambridge, MA 02138, USA. <sup>2</sup>Max Planck Institute for Chemical Physics of Solids, 01187 Dresden, Germany.

<sup>3</sup>Department of Physics, University of Basel, Klingelbergstrasse 82, Basel CH-4056, Switzerland. <sup>4</sup>Weizmann Institute of Science, Rehovot 76100, Israel.

<sup>5</sup>Present address: Northrop Grumman Mission Systems, Linthicum, MD 21090, USA. <sup>6</sup>These authors contributed equally: Shaowen Chen, Seunghyun Park.

✉ e-mail: [shaowenchen@g.harvard.edu](mailto:shaowenchen@g.harvard.edu); [yacoby@g.harvard.edu](mailto:yacoby@g.harvard.edu)

Here we quantitatively visualize the current flow in a JJ device with nanoscale resolution. The spatial distribution of Josephson current flow can be modulated by varying the SC phase difference between two sides of the junction. In any JJ, the SC phase difference is governed by three factors: (i) external magnetic field; (ii) external bias current; (iii) self-field or SC phase gradient induced by the finite Josephson current density. Our measurements reveal the evolution of Josephson current flow with all three factors, including features associated with the change of the number of current loops at the junction known as the Josephson vortex (JV). In particular, factors (i) and (ii) can affect (iii), altering the super current flow even without detectable transport features. We find two previously unidentified effects of the Josephson current-induced phase from factor (iii). First, hidden ground states with different numbers of JVs are found within the zero-resistance state, which can be electrically switched below the critical current. Second, a new mechanism for the Josephson diode effect is established based on the second harmonic phase terms induced by the Josephson current when time-reversal and inversion symmetry are broken.

The measurement setup is shown in Fig. 1a. We employ a diamond tip containing a single nitrogen vacancy (NV) center to map the local magnetic field generated by the current flow<sup>28</sup>. The results are obtained from two devices with junction width  $W=0.15$  and  $0.2\mu\text{m}$ , length  $L=1.5\mu\text{m}$  and thickness  $t=35\text{ nm}$ . The SC electrodes are measured to be in the thin-film limit  $L \ll \lambda_p$ , where  $\lambda_p$  is the Pearl length (Supplementary Fig. 1). This suggests the factor (iii) contribution in our device comes from the Josephson current-induced phase associated with the kinetic inductance of the SC film, instead of the self-field

effect. The junctions are diffusive (electron mean free path  $l_{\text{mfp}} < W$ ) and over-damped (no hysteresis during bias current sweeps). Throughout the paper, we refer to the transverse (longitudinal) direction as  $x(y)$ , and the direction perpendicular to the plane as  $z$ . The origin  $x=y=0$  is set to the center of JJ.

## Results

### current-induced phase

The Josephson current density can be modeled by the sinusoidal current-phase relation<sup>22</sup>

$$J_y(x) = J_c \sin[\phi(x)], \quad (1)$$

where  $J_c$  is the Josephson critical current density (assumed constant for now), and  $\phi(x)$  is the phase difference across the JJ at position  $x$ .  $\phi(x) = \phi_e(x) + \phi_{\text{bias}}$ , where  $\phi_e(x)$  arises from the external magnetic field  $B_z$  (factor i), and  $\phi_{\text{bias}}$  is the additional phase difference due to the injected bias current (factor ii). The strength of Josephson current-induced phase (factor iii) is regulated by  $J_c$ . For small  $J_c$ , the Josephson penetration length  $\lambda_J \approx \sqrt{\Phi_0 L t / 4\pi\mu_0 J_c \lambda_L^2} \gg L$ <sup>29</sup>, the Josephson current-induced phase can be neglected ("weak junction" limit).  $\Phi_0$  is the flux quantum,  $\lambda_L$  is the London penetration length.

In the weak-junction limit, external  $B_z$  controls the number of JV. The transport critical current  $I_c$  oscillates and reaches zero at nodes  $B_z = \pm B_n$  ( $n$  is integer). It is known as the "Fraunhofer map"<sup>30,31</sup>. In each

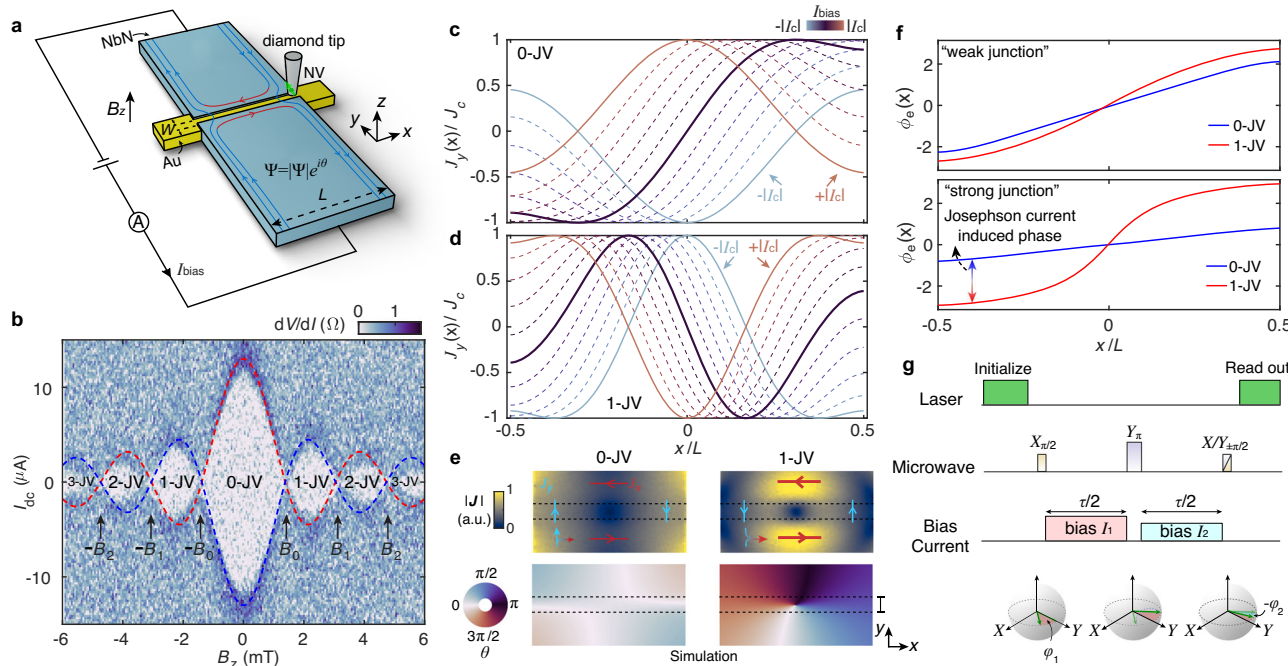


**Fig. 1 | Measurement setup and expected Josephson current flow.** **a** Schematics showing SC-normal-SC junction measured by scanning NV center embedded in a diamond tip. The SC wave function can be described by an amplitude and phase  $\Psi = |\Psi|e^{i\theta}$ . Under external magnetic field  $B_z$ , the screening current near the JJ (red lines) induces a phase difference  $\phi_e(x)$ . The bias current causes a phase difference between the SC electrodes  $\phi_{\text{bias}}$ . **b** Measured differential resistance  $dV/dI$  versus perpendicular magnetic field  $B_z$  and bias current  $I_{\text{dc}}$ , at  $T=7\text{ K}$ . Dashed lines are the expected critical current (see Supplementary Note 2), where red is  $\phi_{\text{bias}} = \pi/2$ , blue is  $\phi_{\text{bias}} = -\pi/2$ . The  $I_c$  nodes are denoted as  $\pm B_n$ . **c, d** Calculated Josephson current normalized by critical current density for 0- and 1-JV states, at external  $B_z=1.0\text{ mT}$  in (c), and  $B_z=1.91\text{ mT}$  in (d). The current flow is sine-like at zero bias current (bold lines), shifts along  $x$  direction at a finite bias current, and becomes cosine-like at the

critical current. **e** Simulations showing the Josephson current flow (top) and local SC phase (bottom) of the 0- and 1-JV states. The screening current near the junction  $J_x$  (red arrows) is reduced by the Josephson current  $J_y$  (cyan arrows) in the 0-JV state, and enhanced in the 1-JV state. This causes the Josephson current-induced phase.  $I_{\text{bias}} = 0$ ,  $B_z \approx 1.2\text{ mT}$  in this simulation. **f**, Simulated  $\phi_e(x)$  for 0- and 1-JV states, at the same  $B_z$  as (e).  $\phi_e(x)$  is the difference of  $\theta$  taken along the two dashed lines in each sub-panel of (e). **g** NV control and current bias sequence based on the ac magnetometry protocol. The X(Y) microwave (MW) pulses rotate the qubit around the X(Y) axis by  $\frac{\pi}{2}$  or  $\pi$ . NV qubit is put on the equator of the Bloch sphere and rotated by the magnetic field generated by current flow. Pulses of different bias current are synced with the MW pulses such that the final signal is the difference between the two current flow patterns.

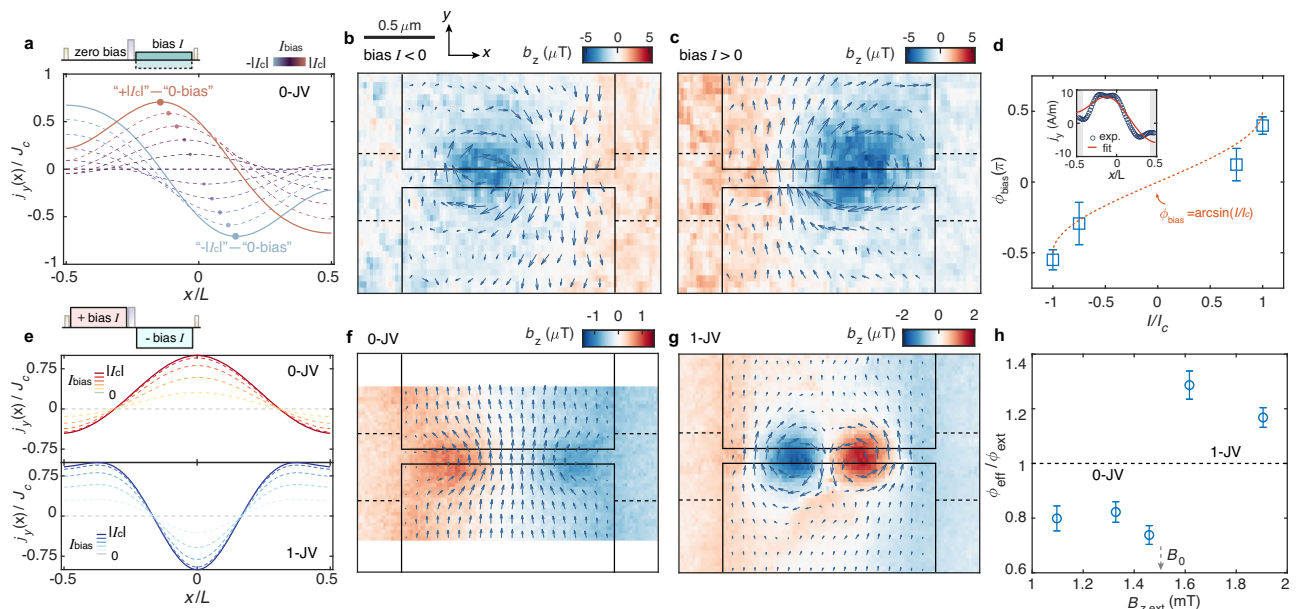


**Fig. 2 | Visualizing Josephson current response to bias current and magnetic field.** **a** Top sketch shows the measurement sequence that takes the difference between zero and finite current bias. Expected current flow show changing line shapes at various bias current  $I_{\text{bias}}$ , with the opposite bias current leading to inverted current flow pattern around the center of the junction. **b, c** Color map shows  $z$ -component of the current-generated magnetic field  $b_z$ . The arrows show the reconstructed current flow vector. Results are measured using the sequence shown in (a). External magnetic field is  $B_z = 0.95$  mT. The SC electrodes are marked by solid lines and normal metal part is marked by dashed lines. **d** Phase difference caused by bias current  $\phi_{\text{bias}}$  extracted from the current flow profile at the junction. The result agrees with the sinusoidal current-phase relation. Inset shows the measured  $j_y(x)$  at  $I_{\text{bias}} = I_c$ , and the fitting results using Supplementary Eqn. 10.

The data in the gray area is excluded in the fitting. **e** Top sketch shows the measurement sequence that takes the difference between symmetric positive and negative  $I_{\text{bias}}$ . The expected signals change sign when measuring the 0- and 1-JV states at their respective  $|I_c|$ . All signals show cosine-like shape, with amplitude growing with  $I_{\text{bias}}$ . **f, g**  $b_z$  and current flow vector maps measured using the sequence shown in (e). The Josephson current changes sign between 0- and 1-JV states. External magnetic field is  $B_z = 1.10$  mT in (f), and  $B_z = 1.91$  mT in (g). **h** Effective phase difference across the junction  $\phi_{\text{eff}} = \phi_{\text{el}-w/2}$  deviates from the external field contribution  $\phi_{\text{ext}}$  (indicated by the shaded area), as a result of induced phase from the Josephson current. Scale bar is 0.5  $\mu\text{m}$  for (b, c, f, g). The measurements are taken at  $T = 7$  K. Error bars in **d** and **h** represent standard deviation from fitting.

lobe where  $B_{n-1} < |B_z| < B_n$ , there are  $n$  JVs at the junction; in the central lobe there is 0-JV (Fig. 1b); the only way to change the number of JV is by sweeping  $B_z$  through the nodes  $B_n$  (Supplementary Fig. 2). In weak junctions the first term  $\phi_e(x)$  is induced by the screening current  $J_x$  in the SC electrodes, and scaled by  $\phi_{e0} \equiv \phi_{\text{el}-L/2} \approx 1.7B_zL^2/\Phi_0$ <sup>31</sup> (Supplementary Eqn. 9). The second term  $\phi_{\text{bias}}$  changes from  $-\pi/2 + n\pi$  to  $\pi/2 + n\pi$  when  $I_{\text{bias}}$  sweeps from  $-|I_c|$  to  $+|I_c|$  (Fig. 1c, d), which can be viewed as moving the JV along the  $xx$  direction.

In “strong junctions” ( $\lambda \ll L$ ),  $\phi(x)$  is altered by the Josephson current-induced phase and lacks analytical solutions. Qualitatively, the screening current  $J_x$  deviates from the weak-junction limit by an amount proportional to the Josephson current  $J_y$  (Fig. 1e), due to the continuity of current. This leads to additional phase gradient  $\partial\theta/\partial x \propto \mathcal{L}_k J_x$ , which changes  $\phi_e(x) = \theta(x)|_{y=W/2} - \theta(x)|_{y=-W/2}$ . Here  $\mathcal{L}_k$  is the kinetic inductance, which is inversely proportional to the superfluid stiffness.  $\theta$  is the SC phase. Specifically, the larger  $J_x$  in the 1-JV state leads to enhanced  $\phi_{e0}$ , compared to the 0-JV state at the same external magnetic field (Fig. 1f).  $I_{\text{bias}}$  can further change the Josephson current and its induced phase. Thus in strong junctions, the total  $\phi(x)$  and current flow need to be solved self-consistently. We find that our device is close to the weak-junction limit at  $T = 7$  K, but is in an intermediate range at  $T = 4$  K.

### Visualizing Josephson current flow

To optimize magnetic field sensitivity, we utilize the “ac magnetometry” protocol, synchronizing NV control pulses with the signal (Fig. 1g). In this protocol, different bias currents  $I_1$  and  $I_2$  is applied to the junction during two halves of each cycle. The magnetic field generated by  $I_k$  rotates the prepared NV spin superposition state along the equator of the Bloch sphere by an angle  $\varphi_k = 2\pi\gamma_e b_{\text{nv}}\tau/2$ , where  $\gamma_e$  is the gyromagnetic ratio of electron spin,  $b_{\text{nv}}$  is the magnetic field projected

along NV axis, and  $\tau$  is cycle duration. After the sequence, the accumulated angle is  $\varphi_1 - \varphi_2$  so each measurement records the *difference* between two selected scenarios.  $b_{\text{nv}}$  is converted to vector components of the magnetic field  $b_{x,y,z}$  using a Fourier method (see Methods). The current vector  $(j_x, j_y)$  is then reconstructed with the Fourier method using in-plane components of the magnetic field. We find similar results with regularization and machine learning methods (see Supplementary Note 5).

We start at  $T = 7$  K where the transport result suggests a weak junction (Fig. 1b). To visualize the evolution of Josephson current, we use two types of sequences. In the first sequence, we highlight the effect of  $\phi_{\text{bias}}$  by taking the difference between finite and zero  $I_{\text{bias}}$  (schematics in Fig. 2a). The expected current profiles  $j_y(x)$  are shown in Fig. 2a, by subtracting the relevant lines in Fig. 1c. The sign of  $I_{\text{bias}}$  determines the direction of the profile shift and the amplitude determines the amount of the shift. Fig. 2b, c show measurements using  $I_{\text{bias}} \approx \pm|I_c|$  in the sequence while no JV is in the junction. As expected, current features are seen at the opposite side of the junction for  $\pm I_{\text{bias}}$ .  $j_y(x)$  at the junction also shows the lateral movement when sweeping  $I_{\text{bias}}$  (Supplementary Fig. 3).  $\phi_{\text{bias}}$  can be acquired by fitting  $j_y(x)$  to the calculated profiles from Fig. 2a (Supplementary Eqn. 10). The result agrees with the sinusoidal current-phase relation (Fig. 2d).

Next we show the effect of magnetic flux on the Josephson current by taking the difference between  $\pm I_{\text{bias}}$  (schematics in Fig. 2e). Here the expected signals are cosine-like and only grow in amplitude with  $I_{\text{bias}}$  (Fig. 2e). For the same  $I_{\text{bias}}$  direction, the signal flips sign for 0- and 1-JV states (switching from red to blue branch in Fig. 1b). Measurements using this sequence are shown in Fig. 2f, g, where we use  $I_{\text{bias}} \approx |I_c|$  in both cases. Results measured at  $I_{\text{bias}} \approx 0.5|I_c|$  show the same shape with half the amplitude (Supplementary Fig. 5a, b). We repeat the

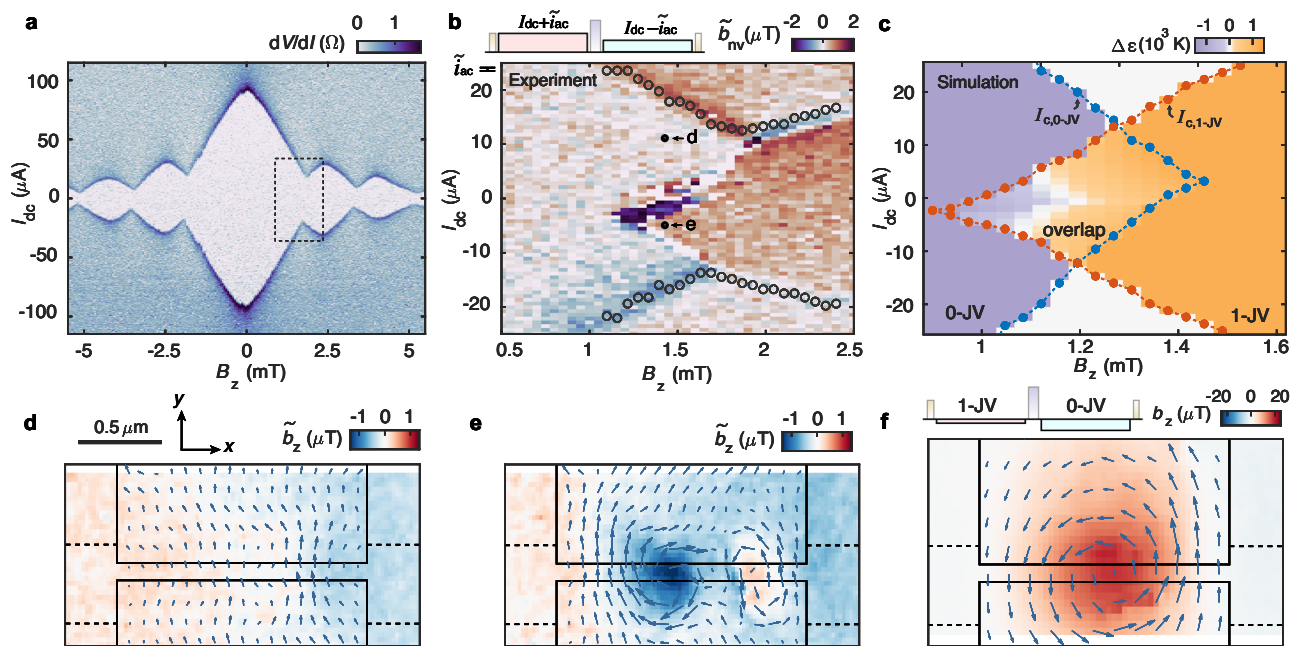


**Fig. 3 | Electric control of JV ground state below critical current.** **a** Differential resistance  $dV/dI$  measured in the same device as Fig. 1c but at  $T = 4$  K, showing order-of-magnitude increase and oscillation of  $I_c$  that does not reach zero. The dashed box shows the measurement range in **(b)**. **b** Top sketch shows measurement sequence. Main panel shows the differential magnetic field projected along NV axis  $\tilde{b}_{nv}$ , generated by the current flow response to the small ac current  $\tilde{i}_{ac} \approx 0.8 \mu\text{A}$ .  $\tilde{b}_{nv}$  is shown versus dc bias current  $I_{dc}$  and perpendicular magnetic field  $B_z$ . The NV is fixed at  $(x, y) \approx (-500, 0)$  nm, where  $x = y = 0$  is the center of JJ. Circles are critical current extracted from transport result in **(a)**. **c** Difference of Gibbs free

energy between the 0- and 1-JV states below  $I_c$ ,  $\Delta\epsilon = \epsilon_{0V} - \epsilon_{1V}$ , from TDGL simulations. Blue (red) circles show simulated critical current of state with 0- (1-) JV. The color in the non-overlap region is saturated to indicate only 0- and 1-JV state is present. **d, e** Spatial maps of differential  $\tilde{b}_z$  and current flow vector measured with sequence shown in **(b)**, showing both **(d)** 0-JV, and **(e)** 1-JV states at the same external field  $B_z = 1.4$  mT. The features in **e** are positioned asymmetrically because the JV is at right-of-center of the junction due to finite  $I_{dc}$ . **f** Full vortex profile is observed when using a sequence that takes the difference between 0- and 1-JV states.

measurement at various magnetic fields, and the current profile reversal can be seen when external  $B_z$  crosses the node  $B_0 \approx 1.5$  mT, i.e., when JV number changes by 1 (Supplementary Fig. 4). Notably, the current flow at  $x = 0$  is parallel (anti-parallel) to  $I_{bias}$  when the junction contains even (odd) number of JVs. In the 2-JV state, the current flow at  $x = 0$  and bias current are both positive (Supplementary Fig. 6), like the 0-JV state (Fig. 2f).

Our measurements provide quantitative details of the current flow compared to previous methods<sup>24,32–34</sup>. First, we confirm the SC is in the thin-film limit ( $L \ll \lambda_p$ ). The absolute value of  $\lambda_p \approx 13 \mu\text{m}$  at  $T = 7$  K is directly measured from the stray field (Supplementary Fig. 1). In comparison, indirect measurements of  $\lambda_p$  range from 1 to 5  $\mu\text{m}$  (see Methods), and thus are unable to determine whether the SC is in the thin-film regime. Second, the JV extends into the SC electrode on both sides by  $\sim 350$  nm (Supplementary Fig. 5c), consistent with the effective area expected from the nodes  $B_n$ . However, the measured  $j_y(x)$  profile does not match the expectation under external  $B_z$ . For example, at  $B_z = 1.1$  mT the  $j_y(x)$  in Fig. 2f is expected to be negative at  $x = \pm L/2$ , but stays positive in the experiment, suggesting a smaller than expected  $\phi_{eo}$  (Supplementary Fig. 4f).

We introduce an effective phase difference  $\phi_{eff}$  as a fitting parameter for the measured  $j_y(x)$ , replacing the theoretically predicted  $\phi_{eo}$  (Supplementary Eqn. 11). Fig. 2h shows  $\phi_{eff}$  is lower (higher) than the phase induced by the external field  $\phi_{ext}$  when  $B_z < B_0$  ( $B_z > B_0$ ). The discrepancy is a direct consequence of the Josephson current-induced phase, as expected in strong junctions. While we find  $\lambda$  is comparable to  $L$  when calculated using experimentally measured parameters, no strong junction feature is observed in the “Fraunhofer map” (Fig. 1b). The Josephson current-induced phase only causes small changes to  $I_c$ , and the effect cancels out when tracking  $I_c$  over large range of  $B_z$ <sup>32</sup>. However, such an effect is still pertinent to designing SC devices such as JJ arrays because the inductance of each junction is affected by the supercurrent flow<sup>35</sup>.

### Electrically switching JV below $|I_c|$

The “Fraunhofer map” changes when measured at  $T = 4$  K. The nodes of  $|I_c|$  at  $B_n$  are lifted although sharp kinks remain (Fig. 3a). This could be caused by a combination of reasons, including an asymmetric critical current density,  $J_c(x) \neq J_c(-x)$  and the strong junction effect due to the increased  $|I_c|$ <sup>33,36,37</sup>. However, the precise mechanism remains difficult to dissect owing to the zero-resistance below  $I_c$ . Here the origin of non-zero local minima of  $|I_c|$  is revealed by mapping the current flow. A differential magnetic field  $\tilde{b}_{nv}$  is measured using a sequence that senses the small ac bias ( $\tilde{i}_{ac}$ ) response while fixing the dc bias ( $I_{dc}$ ), shown by the schematic drawing above Fig. 3b. The  $\tilde{b}_{nv}$  is measured around the kinks of  $|I_c|$  while the NV is fixed over the center of the junction (Fig. 3b main panel). Abrupt changes of  $\tilde{b}_{nv}$  at large  $|I_{dc}|$  match the transport  $I_c$  (circles in Fig. 3b). This suggests that the junction is minimally perturbed by the NV magnetometer.

An additional sharp boundary of  $\tilde{b}_{nv}$  below  $I_c$  separates the 0- and 1-JV states. This is confirmed by the spatial maps in Fig. 3d, e. In Fig. 3d (0-JV state), the current is almost uniform despite being measured at higher external  $B_z$  than Fig. 2f, suggesting  $\phi_{eo}$  is strongly suppressed by the Josephson current-induced phase. Intriguingly, the 0- and 1-JV states can be reached at the same  $B_z$  but different  $I_{bias}$  (Fig. 3d, e). Measuring the difference between two such  $I_{bias}$ , the current profile that corresponds to the JV number changing by 1 is observed (Fig. 3f). This demonstrates precise JV number control using pure electric means while staying below  $I_c$ , which could be useful for low-dissipation memory and logic devices based on SC hybrid structures.

The phase boundary below  $I_c$  supports Josephson current-induced phase as the primary reason for the node-lifting in our device. The induced phase enables the co-stability of the 0- and 1-JV states originating from the existence of two local minima of the energy as a function of the order parameter  $\Psi(\mathbf{r})$  at the same external magnetic field, as shown by the time-dependent Ginzburg-Landau (TDGL)

simulation (Fig. 3c, for details see Supplementary Note 8). The overlapping states with different number of JVs were predicted to arise from the self-field effect previously<sup>38–42</sup>. However, we do not expect self-field to be the main effect here. The measured self-field of the current is insignificant in our device (less than 5% of the external field), and the SC is still in the thin-film limit at  $T = 4$  K ( $L \ll \lambda_p$ , see Methods). Furthermore, the boundary of the 0- and 1-JV phase diagram only extends from the 1-JV region (Fig. 3b) in the experiment. This is independent of sweeping directions of  $B_z$  or  $I_{dc}$  (Supplementary Fig. 9a), and similar behavior is observed between the 1- and 2-JV states (Supplementary Fig. 9b). The lack of hysteresis is quite unexpected. One possibility is that the JJ relaxes to the ground state with lower energy due to the elevated temperature and small perturbations of the measurement, although the detailed mechanism is an open question for future work. The simulated Gibbs free energy difference  $\Delta\epsilon = \epsilon_{0V} - \epsilon_{1V}$  shows the 1-JV state has lower energy than the 0-JV state in most, but not all of the overlap region (Fig. 3c). In fact, including the self-field effect energetically favors the 0-JV over the 1-JV state, further deviating from the experimental results (Supplementary Fig. 20).

### Inversion asymmetry and Josephson diode effect

The transport  $I_c$  is non-reciprocal when  $I_{bias}$  is applied in opposite directions at  $T = 4$  K, i.e.  $|I_c^+| \neq |I_c^-|$  (Fig. 4a). This is referred to as the “Josephson diode effect”<sup>43</sup>. The asymmetry parameter,  $\eta = \frac{|I_c^+| - |I_c^-|}{|I_c^+| + |I_c^-|}$ , exceeds 10% in our device. We identify a new mechanism for the diode effect comprising three ingredients, (i) time-reversal symmetry breaking (by  $B_z$ ), (ii) inversion symmetry breaking, and (iii) Josephson current-induced phase. The first two conditions are required by symmetry<sup>17,44</sup>, while the third provides a mechanism whereby the Josephson current is not a simple sinusoidal function of  $\phi_{bias}$ . As a result, the critical current density is reached on opposite sides of the junction at  $\pm I_{bias}$ , which leads to asymmetric  $I_c^\pm$  (Fig. 4b). Interestingly, it can be shown theoretically that first two ingredients alone are not sufficient to generate the diode effect Supplementary Note 7. Combining the symmetry breaking with the Josephson current-induced phase introduces higher harmonic terms with a phase offset in the current-phase relation Supplementary Note 7. Our results confirm all three components are necessary. For example, the current profile measured at  $T = 7$  K is asymmetric,  $j_y(x) \neq j_y(-x)$ , suggesting broken inversion symmetry (Supplementary Fig. 16). However, the weaker current-induced phase due to smaller  $J_c$  is insufficient to generate a non-reciprocal global critical current response (Supplementary Note 6).

The current flow measurement directly reveals the broken inversion symmetry even when the global  $I_c^\pm$  is almost symmetric. The  $\tilde{b}_{nv}$  map at  $\pm I_{bias}$  is measured at  $B_z = 0.5$  mT. Although  $\eta$  is only about 2%, the current flow pattern is clearly asymmetric for  $\pm I_{bias}$ ; a loop appears near the left edge for  $-I_{bias}$  (Fig. 4c) but not for  $+I_{bias}$  (Fig. 4d). We model the non-uniform  $J_c(x)$  with an uneven junction width  $W$  ( $W_1 > W_2$ ) in the TDGL simulation, confirming the role of broken inversion symmetry (Fig. 4e, f); if the junction is inversion symmetric, the ac current flow for  $\pm I_{bias}$  should be mirrored along the  $x$  direction (Supplementary Fig. 21f–h). In fact, the broken inversion symmetry is also responsible for the skewed phase boundary for  $\pm I_{bias}$  in Fig. 3b, c. In reality, the non-uniform  $J_c(x)$  could be due to variations in junction width, SC/normal barrier transparency, or normal metal resistivity.

## Discussion

The JV discussed in our work should be distinguished from the Abrikosov vortex in type-II superconductors<sup>45</sup>. While both move in the same direction with  $I_{bias}$  and exhibit normal cores, observed in spectroscopic studies<sup>18,46</sup>, only the JV configuration can be controlled by a small change of  $I_{bias}$  below  $I_c$ . Even when the current-induced phase is weak, the JV can be precisely moved side-to-side by the small change of  $I_{bias}$  from  $-|I_c|$  to  $|I_c|$  at  $B_z = B_n \pm \epsilon$ , ( $\epsilon \ll 1$ ). In particular,  $|I_c|$  should vanish at  $B_z = B_n$ , if the junction is symmetric about its midpoint. This control over the JV

position enables us to observe the large alternating magnetic field signal at the JJ with minimal changes in  $I_{bias}$  (Fig. 2g). Finally, the minimal energy cost associated with JV movement ( $I_c \Delta\phi$ ) as  $I_c \rightarrow 0$  supports JV control as an energy-efficient way of communication between qubits<sup>47</sup>.

The new mechanism of the Josephson diode effect offers a blueprint to realize a scalable SC rectifier with any thin-film SC. Conventional Josephson diodes that are driven by the self-field effect require a large operating current because the geometric inductance is usually small, especially at the nanoscale<sup>48,49</sup>. However, the kinetic inductance can dominate in SC with small superfluid stiffness (e.g., low superfluid density), making it possible to reduce the device size. This also enables electric tuning of the Josephson diode by injecting a small current  $J_x$  to control the Josephson current-induced phase.

Finally, spatial mapping of the current flow  $J(x, y)$  presents an alternative observable to electrical transport in SC hybrid structures. By accurately measuring  $J(x, y)$  with high sensitivity and spatial resolution, we pinpoint the origin of the Josephson diode effect in our device, which is otherwise hidden. Our approach opens up further avenues to unseal the mechanisms for the non-reciprocity in a broad range of SC systems, and symmetry breaking in gate-tunable superconductors based on van der Waals and moiré materials. The measured current flow could be directly compared with simulations based on TDGL or quantum transport to diagnose SC circuits, such as the local transparency of the JJ barrier.

## Methods

### Variable temperature scanning setup

Measurements were performed in a home-built variable temperature system with optical access. There are multiple nano-pillars containing NV centers on each diamond probe, and a goniometer with both pitch and yaw control is used to set the stand-off distance between the NV and the sample<sup>28</sup>, which ranges between 130 to 180 nm throughout the study. The NV center is excited with 532 nm green laser (Coherent Sapphire), and read out with standard optical detected magnetic resonance (ODMR) technique using a 600 nm long-pass optical filter. The time-averaged power of the green laser pulses is less than 50  $\mu$ W. The microwave (MW) drive is provided via on-chip transmission line next to the sample. MW is sourced from SGS-100A (Rohde & Schwarz) and modulated with the built-in IQ mixer. MW pulses are then amplified by +40 db using 30S1G6C (AR Inc), and routed through another switch (RF lambda) to reduce noise from the amplifier. MW and bias current control sequences are generated by arbitrary wave generator AWG5014C (Tektronix).

### Device fabrication and electrical characterization

The SC and normal parts of the JJ are made of niobium nitride (NbN) and gold (Au) thin films, respectively. The JJs are fabricated on undoped Silicon substrate with 285 nm SiO<sub>2</sub> on top. Standard electron beam lithography method is used to define the device geometry using double-layer e-beam resist. The normal part of the junction is first formed with thermal evaporation (2 nm Ti/ 35 nm Au). A short Argon milling process is used right before sputtering SC electrodes (2 nm Ti/ 6 nm Nb/ 30 nm NbN). The MW strip line is formed with 2 nm Ti/ 60 nm Au. Four terminal resistance result was first measured with dc bias from Keithley 2400 and dc voltage with Keithley 2100, and then taken numerical derivative to acquire differential resistance shown in the main text.

### Probe fabrication and typical characteristics

The diamond fabrication process follows ref. 50. Specifically, ultra pure diamond with natural 13C abundance and [100] facet (electronic grade from Element Six) is diced into thin slabs ~50  $\mu$ m thick. One side of the slab is etched by Argon/Chloride plasma to relieve surface strain, then implanted with 15N ions at a dose of  $5 \times 10^{10}/\text{cm}^2$  and acceleration energy of 6 keV (Innovion). Then the diamond is annealed in ultrahigh vacuum ( $< 3 \times 10^{-8}$  Torr) at 800 °C for 24 hours to form NV centers. The diamond nano-pillars are defined with standard e-beam lithography

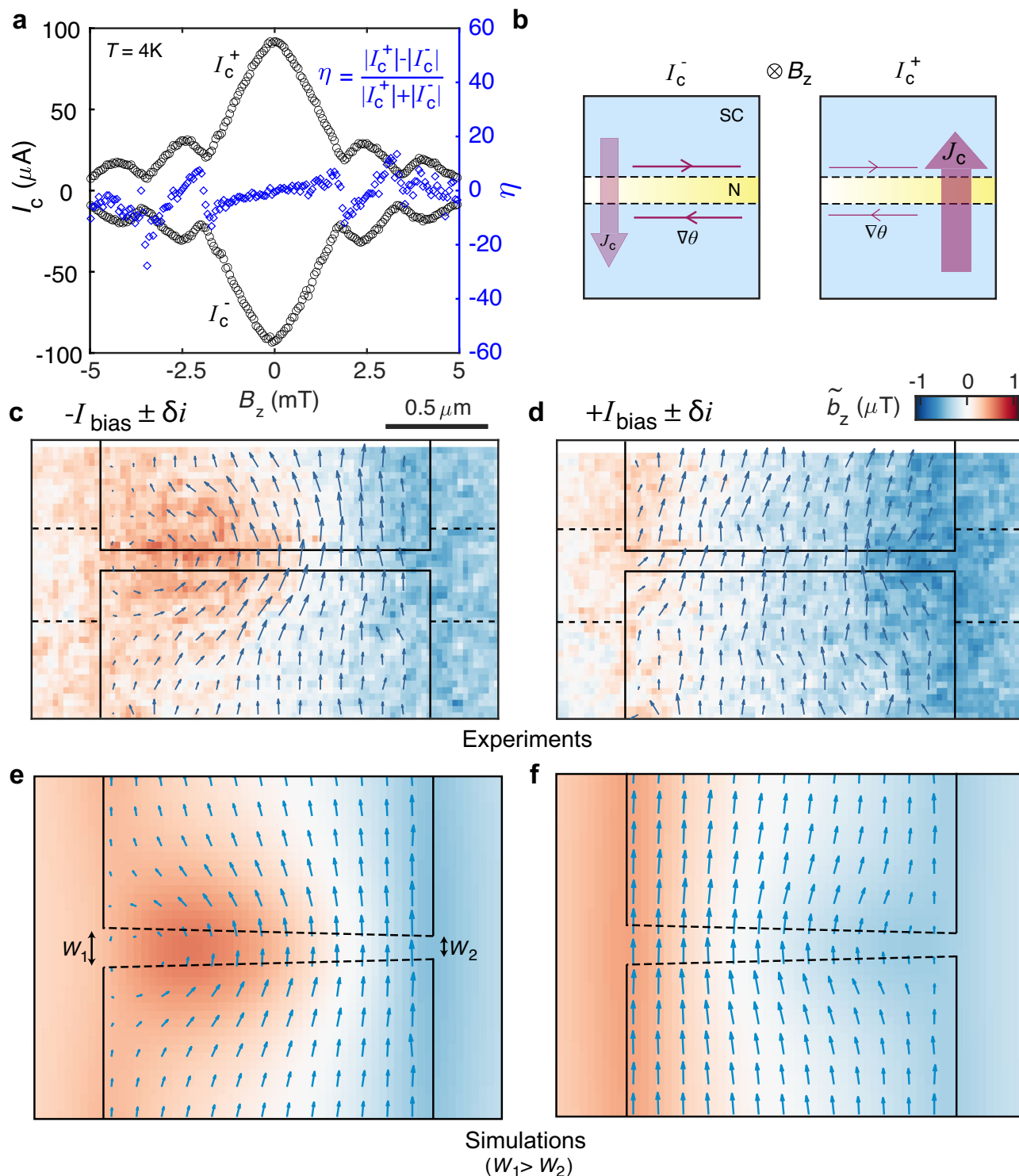


**Fig. 4 | A new mechanism for the Josephson diode effect.** **a** Left axis, forward and backward critical current extracted from results measured in Fig. 3a. Right axis, asymmetry parameter  $\eta$  showing JDE when time-reversal symmetry is broken by  $B_z$ . **b** Schematics showing inversion symmetry breaking (non-uniform  $J_c$ ) at the junction can lead to different forward and backward critical current. **c, d** Differential

magnetic field  $\tilde{b}_z$  and current flow vector measured at symmetric  $\pm I_{\text{bias}}$  show inversion asymmetric patterns. Measurements are taken at  $B_z = 0.5 \text{ mT}$ , using the same sequence as described in Fig. 3b. **e, f** Simulated results corresponding to (c) and (e), when inversion symmetry at the junction is broken, modeled as non-uniform junction width  $W_1 > W_2$ . The measurements in (a, c, d) are taken at  $T = 4 \text{ K}$ .

and etched with  $\text{O}_2$  plasma. On average we get 1 NV center per diamond pillar with this process. The NV depth from the surface is about 15–20 nm. Typical ODMR red photon count is 100 k/s, contrast in pulsed measurement is 20 to 30%, and the coherence time is  $T_2 \approx 1 \mu\text{s}$  and  $T_2 \approx 30 \mu\text{s}$  at 4 K and the small magnetic field used in this study.

#### Detail about NV magnetometry

NV is a spin-1 system with low energy states  $s = |0\rangle, |\pm 1\rangle$ . The  $|0\rangle$  is split in energy from  $|\pm 1\rangle$  by the zero field splitting (2.87 GHz) and  $|\pm 1\rangle$  are further split by the Zeeman energy  $E_Z = g\mu_B B_{\text{nv}}$ , here  $g = 2$  is the Landé g-factor for electron,  $\mu_B$  is the Bohr magneton, and  $B_{\text{nv}}$  is the magnetic

field along NV axis. In practice, we apply a external field of less than 50 G along the NV axis, and drive the  $|0\rangle$  and  $|-\rangle$  states as a qubit using MW. As mentioned in the main text, “ac” magnetometry is used to filter out low frequency noise and maximize sensitivity by utilizing the longer  $T_2$  coherence time. Specifically, the NV qubit is first prepared in the  $|0\rangle$  state using a green laser pulse, and then driven into the superposition state  $\frac{1}{\sqrt{2}}(|0\rangle + |-\rangle)$  by a  $X_{\frac{\pi}{2}}$  MW pulse. We use two types of dynamic decoupling sequences, the spin echo (Hahn echo) with one  $\pi$ -pulse, and the Carr-Purcell-Meiboom-Gill (CPMG) with  $n$ - $Y_n$  pulses in the experiment<sup>51,52</sup>. Between neighboring  $\pi$ -pulses, the qubit rotates by an angle  $\varphi = 2\pi\gamma_e b_{\text{nv}}\tau_n$ , where  $\gamma_e = 28 \text{ GHz/T}$  is the gyromagnetic ratio of the electron spin,  $b_{\text{nv}}$  is the magnetic field generated by the current projected along NV axis, and  $\tau_n$  is the evolution time between neighboring MW pulses. The  $\pi$ -pulses reverse the qubit rotation direction, and the total angle is the difference of the accumulation in each half of the sequence. The frequency of NV control sequence and bias current modulation is  $f = 100$  to  $500 \text{ kHz}$ , corresponding to  $<1 \text{ nA}$  bias current due to the AC Josephson effect  $I = h/2eR_N$ <sup>22</sup> ( $h$  is Planck’s constant,  $e$  is electron charge,  $R_N \approx 1\Omega$  is the normal state resistance of the JJ). This is 3 to 4 orders of magnitude smaller than the bias current applied to the JJ.

To extract the phase accumulation angle, the NV spin is projected to the  $|0\rangle$  and  $|-\rangle$  states using four  $\frac{\pi}{2}$ -pulses  $\frac{\pi}{2}_{\pm X/Y}$  and record the ODMR signal. The angle is then calculated from

$$\varphi = \arctan \frac{C_{\frac{\pi}{2}X} - C_{\frac{\pi}{2}-X}}{C_{\frac{\pi}{2}Y} - C_{\frac{\pi}{2}-Y}} \quad (2)$$

where  $C_{\frac{\pi}{2}X/Y}$  are the photon counts from  $\frac{\pi}{2}_{\pm X/Y}$  projections. The measurement sequences are averaged up to 100k times (about 10 seconds) at each point to extract the  $B_{\text{nv}}$ .

### Reconstructing current flow from magnetic field

In this section, we discuss the three methods used to reconstruct current flow  $j_{x,y}$  from  $b_{\text{nv}}$ . For all methods, we first convert the magnetic field projected along NV axis  $b_{\text{nv}}$ , to Cartesian vector magnetic field  $b_{x,y,z}$  using the source-free constraint for the stray field<sup>53-55</sup>,

$$\nabla \times b = 0 \quad (3)$$

Thus in the Fourier space the vector components are,

$$\begin{aligned} b_z(\mathbf{k}) &= \frac{b_{\text{nv}}(\mathbf{k})}{\mathbf{u}_{\text{nv}} \cdot \mathbf{u}} \\ b_x(\mathbf{k}) &= -i \frac{k_x}{k} b_z(\mathbf{k}) \\ b_y(\mathbf{k}) &= -i \frac{k_y}{k} b_z(\mathbf{k}) \end{aligned} \quad (4)$$

here  $\mathbf{k} = (k_x, k_y)$  is the 2D wavevector,  $k = \sqrt{k_x^2 + k_y^2}$ ,  $\mathbf{u}_{\text{nv}}$  is the unit vector of the NV axis,  $\mathbf{u} = (-ik_x/k, -ik_y/k, 1)$ . The singularity point at  $k = 0$  is discarded during the reconstruction. Because the SC electrode is much longer than our measurement window in the  $y$  direction, the  $j_y$  outside the window on the top and bottom sides also contribute to the measured  $b_{\text{nv}}$ . In practice, we extend the measured  $b_{\text{nv}}$  with the top and bottom lines in the  $y$  direction, and linearly extrapolates  $b_{\text{nv}}$  to zero in the  $x$  direction. The padding size in each direction is 10 times of the measurement window, at which point increasing the size does not change the reconstruction result. More detail of the reconstruction process is discussed in Supplementary Note 5.

### Data availability

All experimental and numerically simulated data included in this work are available in the Zenodo database<sup>56</sup>.

### References

- Josephson, B. D. Possible new effects in superconductive tunneling. *Phys. Lett.* **1**, 251–253 (1962).
- de Gennes, P. Boundary effects in superconductors. *Rev. Mod. Phys.* **36**, 225 (1964).
- Josephson, B. Coupled superconductors. *Rev. Mod. Phys.* **36**, 216 (1964).
- Devoret, M. H. & Schoelkopf, R. J. Superconducting circuits for quantum information: an outlook. *Science* **339**, 1169–1174 (2013).
- Fedorov, K. G., Shcherbakova, A. V., Wolf, M. J., Beckmann, D. & Ustinov, A. V. Fluxon readout of a superconducting qubit. *Phys. Rev. Lett.* **112**, 160502 (2014).
- Kjaergaard, M. et al. Superconducting qubits: current state of play. *Annu. Rev. Cond. Matter Phys.* **11**, 369–395 (2020).
- Wang, H. et al. Coherent terahertz emission of intrinsic Josephson junction stacks in the hot spot regime. *Phys. Rev. Lett.* **105**, 057002 (2010).
- Welp, U., Kadowaki, K. & Kleiner, R. Superconducting emitters of THz radiation. *Nat. Photon.* **7**, 702–710 (2013).
- Kirtley, J. R. & Wikswo Jr, J. P. Scanning squid microscopy. *Annu. Rev. Mater Sci.* **29**, 117–148 (1999).
- Kirtley, J. Fundamental studies of superconductors using scanning magnetic imaging. *Rep. Prog. Phys.* **73**, 126501 (2010).
- Holmes, D. S., Ripple, A. L. & Manheimer, M. A. Energy-efficient superconducting computing - power budgets and requirements. *IEEE Trans. Appl. Supercond.* **23**, 1701610 (2013).
- Grosfeld, E. & Stern, A. Observing Majorana bound states of Josephson vortices in topological superconductors. *PNAS* **108**, 11810–11814 (2011).
- Beenakker, C. Search for Majorana fermions in superconductors. *Annu. Rev. Condens. Matter Phys.* **4**, 113–136 (2013).
- Lutchyn, R. M. et al. Majorana zero modes in superconductor–semiconductor heterostructures. *Nat. Rev. Mater.* **3**, 52–68 (2018).
- Pal, B. et al. Josephson diode effect from cooper pair momentum in a topological semimetal. *Nat. Phys.* **18**, 1228–1233 (2022).
- Jeon, K.-R. et al. Zero-field polarity-reversible Josephson supercurrent diodes enabled by a proximity-magnetized pt barrier. *Nat. Mater.* **21**, 1008–1013 (2022).
- Nadeem, M., Fuhrer, M. S. & Wang, X. The superconducting diode effect. *Nat. Rev. Phys.* **5**, 558–577 (2023).
- Roditchev, D. et al. Direct observation of Josephson vortex cores. *Nat. Phys.* **11**, 332–337 (2015).
- Tsuei, C. et al. Pairing symmetry and flux quantization in a tricrystal superconducting ring of  $\text{YBa}_2\text{Cu}_3\text{O}_{7-\delta}$ . *Phys. Rev. Lett.* **73**, 593 (1994).
- Hilgenkamp, H. et al. Ordering and manipulation of the magnetic moments in large-scale superconducting  $\pi$ -loop arrays. *Nature* **422**, 50–53 (2003).
- Gutfreund, A. et al. Direct observation of a superconducting vortex diode. *Nat. Commun.* **14**, 1630 (2023).
- Tinkham, M. *Introduction to superconductivity* (McGraw-Hill, 1996).
- Gross, R. & Koelle, D. Low temperature scanning electron microscopy of superconducting thin films and Josephson junctions. *Rep. Prog. Phys.* **57**, 651 (1994).
- Dremov, V. V. et al. Local Josephson vortex generation and manipulation with a magnetic force microscope. *Nat. Commun.* **10**, 4009 (2019).
- Hovhannисyan, R. A., Grebenchuk, S. Y., Baranov, D. S., Roditchev, D. & Stolyarov, V. S. Lateral Josephson junctions as sensors for magnetic microscopy at nanoscale. *J. Phys. Chem., Lett.* **12**, 12196–12201 (2021).
- Grebenchuk, S. Y. et al. Observation of interacting Josephson vortex chains by magnetic force microscopy. *Phys. Rev. Res.* **2**, 023105 (2020).

27. Stolyarov, V. S. et al. Revealing Josephson vortex dynamics in proximity junctions below critical current. *Nano Lett.* **22**, 5715–5722 (2022).

28. Vool, U. et al. Imaging phonon-mediated hydrodynamic flow in WTe<sub>2</sub>. *Nat. Phys.* **17**, 1216–1220 (2021).

29. Tolpygo, S. K. & Gurvitch, M. Critical currents and Josephson penetration depth in planar thin-film high-*t<sub>c</sub>* Josephson junctions. *Appl. Phys. Lett.* **69**, 3914–3916 (1996).

30. Rowell, J. Magnetic field dependence of the Josephson tunnel current. *Phys. Rev. Lett.* **11**, 200 (1963).

31. Clem, J. R. Josephson junctions in thin and narrow rectangular superconducting strips. *Phys. Rev. B* **81**, 144515 (2010).

32. Dynes, R. & Fulton, T. Supercurrent density distribution in Josephson junctions. *Phys. Rev. B* **3**, 3015 (1971).

33. Mayer, B., Schuster, S., Beck, A., Alff, L. & Gross, R. Magnetic field dependence of the critical current in YBa<sub>2</sub>Cu<sub>3</sub>O<sub>7-δ</sub> bicrystal grain boundary junctions. *Appl. Phys. Lett.* **62**, 783–785 (1993).

34. Holm, J. & Mygind, J. A novel cryogenic scanning laser microscope tested on Josephson tunnel junctions. *Rev. Sci. Inst.* **66**, 4547–4551 (1995).

35. Kuzmin, R., Mehta, N., Grabon, N. & Manucharyan, V. E. Tuning the inductance of Josephson junction arrays without squids. *Appl. Phys. Lett.* **123**, 182602 (2023).

36. Hilgenkamp, H. & Mannhart, J. Grain boundaries in high-*t<sub>c</sub>* superconductors. *Rev. Mod. Phys.* **74**, 485 (2002).

37. Boris, A. A. et al. Evidence for nonlocal electrodynamics in planar Josephson junctions. *Phys. Rev. Lett.* **111**, 117002 (2013).

38. Owen, C. & Scalapino, D. Vortex structure and critical currents in Josephson junctions. *Phys. Rev.* **164**, 538 (1967).

39. Pagano, S., Ruggiero, B. & Sarnelli, E. Magnetic-field dependence of the critical current in long Josephson junctions. *Phys. Rev. B* **43**, 5364 (1991).

40. Kuplevakhsky, S. & Glukhov, A. Static solitons of the sine-gordon equation and equilibrium vortex structure in Josephson junctions. *Phys. Rev. B* **73**, 024513 (2006).

41. Kuplevakhsky, S. & Glukhov, A. Exact analytical solution of the problem of current-carrying states of the Josephson junction in external magnetic fields. *Phys. Rev. B* **76**, 174515 (2007).

42. Kuplevakhsky, S. & Glukhov, A. Exact analytical solution of a classical Josephson tunnel junction problem. *Low. Temp. Phys.* **36**, 1012–1021 (2010).

43. Moll, P. J. & Geshkenbein, V. B. Evolution of superconducting diodes. *Nat. Phys.* **19**, 1379–1380 (2023).

44. Zhang, Y., Gu, Y., Li, P., Hu, J. & Jiang, K. General theory of Josephson diodes. *Phys. Rev. X* **12**, 041013 (2022).

45. Abrikosov, A. A. Magnetic properties of superconductors of the second group. *Sov. Phys.* **5**, 1174–1182 (1957).

46. Hess, H., Robinson, R., Dynes, R., Valles Jr, J. & Waszczak, J. Scanning-tunneling-microscope observation of the Abrikosov flux lattice and the density of states near and inside a fluxoid. *Phys. Rev. Lett.* **62**, 214 (1989).

47. Wallraff, A. et al. Quantum dynamics of a single vortex. *Nature* **425**, 155–158 (2003).

48. Goldman, A. & Kreisman, P. Meissner effect and vortex penetration in Josephson junctions. *Phys. Rev.* **164**, 544 (1967).

49. Golod, T. & Krasnov, V. M. Demonstration of a superconducting diode-with-memory, operational at zero magnetic field with switchable nonreciprocity. *Nat. Commun.* **13**, 3658 (2022).

50. Zhou, T. X., Stöhr, R. J. & Yacoby, A. Scanning diamond NV center probes compatible with conventional AFM technology. *Appl. Phys. Lett.* **111**, 163106 (2017).

51. Biercuk, M., Doherty, A. & Uys, H. Dynamical decoupling sequence construction as a filter-design problem. *J. Phys. B: At. Mol. Opt. Phys.* **44**, 154002 (2011).

52. Pham, L. M. et al. Enhanced solid-state multispin metrology using dynamical decoupling. *Phys. Rev. B* **86**, 045214 (2012).

53. Blakely, R. J. *Potential theory in gravity and magnetic applications* (Cambridge University Press, 1996).

54. Lima, E. A. & Weiss, B. P. Obtaining vector magnetic field maps from single-component measurements of geological samples. *J. Geophys. Res. Solid Earth* **114**, B06102 (2009).

55. Casola, F., Van Der Sar, T. & Yacoby, A. Probing condensed matter physics with magnetometry based on nitrogen-vacancy centres in diamond. *Nat. Rev. Mater.* **3**, 1–13 (2018).

56. Chen, S. & Park, S. Current induced hidden states in Josephson junctions. Zenodo. <https://doi.org/10.5281/zenodo.13256436> (2024).

## Acknowledgements

We thank Y. Xie, J. Cremer, A. Hamo, T. Werkmeister for inspiring discussions. A.Y. acknowledges support from the Army Research Office under Grant numbers W911NF-22-1-0248 and W911NF-21-2-0147, the Gordon and Betty Moore Foundation through Grant GBMF 9468, and the Quantum Science Center (QSC), a National Quantum Information Science Research Center of the U.S. Department of Energy (DOE). S.C. and S.P. acknowledge partial support from the Harvard Quantum Initiative in Science and Engineering. A.S. acknowledges support by the European Union's Horizon 2020 research and innovation program (Grant Agreement LEGOTOP No. 788715), the German Research Foundation DFG (CRC/Transregio 183, El 519/7-1), and the Israel Science Foundation Quantum Science and Technology (2074/19). P.M. acknowledges financial support through SNSF project No. 188521 and through ERC consolidator grant QS2DM. B.I.H. acknowledges support from NSF grant DMR 1231319.

## Author contributions

S.C., S.P., U.V., and A.Y. conceived and designed the experiments; S.C. and S.P. prepared the devices, performed the electrical transport and magnetometry measurements, analyzed and visualized the data with input from U.V., N.M., and A.Y.; S.C., and S.P. carried out the simulation and analysis with input from A.S., B.I.H., and A.Y.; D.A.B., M.F., and P.M. carried out the current reconstruction using machine learning method; T.Z. fabricated the diamond probes; S.C. and S.P. wrote the manuscript with input from U.V., A.S., B.I.H., A.Y., and contributions from all co-authors.

## Competing interests

A.Y., S.C., E.P., U.V., N.M., A.S., and B.I.H. have applied for a patent partially based on this work. The other authors declare no competing interests.

## Additional information

**Supplementary information** The online version contains supplementary material available at <https://doi.org/10.1038/s41467-024-52271-z>.

**Correspondence** and requests for materials should be addressed to Shaowen Chen or Amir Yacoby.

**Peer review information** *Nature Communications* thanks the anonymous reviewers for their contribution to the peer review of this work. A peer review file is available.

**Reprints and permissions information** is available at <http://www.nature.com/reprints>

**Publisher's note** Springer Nature remains neutral with regard to jurisdictional claims in published maps and institutional affiliations.

**Open Access** This article is licensed under a Creative Commons Attribution-NonCommercial-NoDerivatives 4.0 International License, which permits any non-commercial use, sharing, distribution and reproduction in any medium or format, as long as you give appropriate credit to the original author(s) and the source, provide a link to the Creative Commons licence, and indicate if you modified the licensed material. You do not have permission under this licence to share adapted material derived from this article or parts of it. The images or other third party material in this article are included in the article's Creative Commons licence, unless indicated otherwise in a credit line to the material. If material is not included in the article's Creative Commons licence and your intended use is not permitted by statutory regulation or exceeds the permitted use, you will need to obtain permission directly from the copyright holder. To view a copy of this licence, visit <http://creativecommons.org/licenses/by-nc-nd/4.0/>.

© The Author(s) 2024